

Inhomogeneous high temperature melting and decoupling of charge density waves in spin-triplet superconductor UTe_2

Alexander LaFleur^{1,*}, Hong Li^{1,*}, Corey E. Frank², Muxian Xu¹, Siyu Cheng¹, Ziqiang Wang¹, Nicholas P. Butch^{2,3} and Ilija Zeljkovic^{1,§}

¹ Department of Physics, Boston College, Chestnut Hill, MA, USA

² NIST Center for Neutron Research, National Institute of Standards and Technology, Gaithersburg, MD, USA

³ Maryland Quantum Materials Center, Department of Physics, University of Maryland, College Park, MD, USA

* *Authors contributed equally*

§ *Corresponding author: ilija.zeljkovic@bc.edu*

Abstract:

Periodic spatial modulations of the superfluid density, or pair density waves, have now been widely detected in unconventional superconductors, either as the primary or the secondary states accompanying charge density waves. Understanding how these density waves emerge, or conversely get suppressed by external parameters, provides an important insight into their nature. Here we use spectroscopic imaging scanning tunneling microscopy to study the evolution of density waves in the heavy fermion spin-triplet superconductor UTe_2 as a function of temperature and magnetic field. We discover that charge modulations, composed of three different wave vectors gradually weaken but persist to a surprisingly high temperature $T_{\text{CDW}} \approx 10\text{-}12$ K. By tracking the local amplitude of modulations, we find that these modulations become spatially inhomogeneous, and form patches that shrink in size with higher temperature or with applied magnetic field. Interestingly, one of the density wave vectors along the mirror symmetry has a slightly different temperature onset, thus revealing an unexpected decoupling of the three-component CDW state. Importantly, T_{CDW} determined from our work matches closely to the temperature scale believed to be related to magnetic fluctuations, providing the first possible connection between density waves observed by surface probes and bulk measurements. Combined with magnetic field sensitivity of the modulations, this could point towards an important role of spin fluctuations or short-range magnetic order in the formation of the primary charge density wave.

Introduction:

Unconventional superconductivity often occurs in close proximity to other symmetry-breaking phases. In the canonical example of cuprate superconductors, superconductivity is found to co-exist with electronic nematic phase, which breaks the rotation symmetry of the system, and the periodic modulations, or waves, of the charge density and the superfluid density throughout much of the phase diagram ¹. The Cooper pair density waves (PDWs), either as the primary drivers or as secondary states accompanying charge density waves (CDWs), have now been seen in a range of unconventional superconductors, including cuprate high-temperature superconductors ²⁻⁴, Fe-based superconductors ^{5,6} and kagome superconductors ⁷⁻⁹.

Out of the array of density wave superconductors, heavy fermion superconductor UTe_2 is an intriguing example of a system that also shows strong evidence for spin-triplet superconductivity in proximity to an underlying magnetic instability^{10,11} and strong fluctuations^{12–15}. Unconventional pairing is supported by the very small Knight shift change across the bulk superconducting transition temperature T_c ^{10,16}, large and highly anisotropic critical magnetic fields¹⁰, peculiar phase diagram with multiple superconducting regimes¹⁷ and the non-zero polar Kerr effect below T_c ¹² signaling time-reversal symmetry breaking despite the absence of long-range magnetic order¹⁰. Within this superconducting state, the system is also reported to host intertwined Cooper pair and charge density wave modulations^{18,19}, further highlighting the unusual nature of this superconductor. Understanding how these phases onset as the temperature is lowered, or how they are suppressed by perturbations such as magnetic field or chemical doping can provide an essential insight into their nature.

Here we use spectroscopic imaging scanning tunneling microscopy (SI-STM) to investigate the evolution of charge modulations in UTe_2 as a function of temperature and magnetic field. We find that the CDW phase persists substantially above the superconducting transition, reaching about 10–12 K. SI-STM spatial mapping reveals that the CDW phase is suppressed by forming short-range CDW regions that shrink in size as the CDW approaches global suppression, by either increasing the temperature or applying magnetic field. The arrangement of CDW puddles is reproducible with repeated thermal or field cycles, pointing towards the role of local disorder. Interestingly, based on the temperature and energy-dependence, we discover one of the density wave vectors along the mirror symmetry direction is distinct compared to the other two. This reveals an unexpected decoupling of the three-component CDW state that should be pursued in future theoretical work. The onset temperature of charge modulations observed here closely matches the temperature scale in transport measurements associated with magnetic fluctuations, providing the first plausible connection relating the density waves observed by surface sensitive experiments and bulk measurements. Given this agreement in temperature scales, combined with our observation of magnetic field sensitivity of the CDW in the normal state, our work motivates exploring the origin of CDW related to magnetic fluctuations.

Results:

We study bulk single crystals of UTe_2 with bulk superconducting $T_{SC} \approx 1.6$ K¹⁰ (Methods). We cleave the crystals in ultra-high-vacuum at liquid nitrogen temperature, and immediately insert them into the microscope head. The crystal structure of UTe_2 is orthorhombic and UTe_2 crystals tend to cleave along the [0-11] direction^{18–20}. Typical STM topographs of the (0-11) plane show a chain-like surface, with two rows of Te atoms oriented along the [100] direction (Fig. 1a), similarly to what has been observed in other STM studies^{18–20}. In addition to the atomic Bragg peaks Q_{Bragg} and Te chain Bragg peaks Q_{chain} (Fig. 1b), Fourier transforms (FTs) of differential conductance dI/dV maps show three other pairs of peaks (Fig. 1c,d). These peaks are non-dispersive with energy (Fig. 1e-g) and correspond to an emergent charge density wave (CDW) intertwined with a PDW at the same wave vectors^{18,19}.

Previous STM experiments primarily focused on studying these density waves in the superconducting state, and reported their existence up to at least 4.2 K^{18,19}. Consistent with these, CDW peaks in our data are also clearly detectable at 4.2 K (Fig. 1d). We proceed to investigate how the CDW state disappears, first exploring the effect of increasing the temperature. We measure and compare dI/dV maps as a function of temperature over an identical area of the sample, acquired under the same experimental conditions (Fig. 2a-d). To quantitatively evaluate the evolution of the CDW phase, we extract FT linecuts

from the center of the FT through each of the three CDW peaks at every temperature measured (Fig. 2a-c). It can be seen that peaks get progressively suppressed with temperature. At maximum temperature used in this experiment sequence of 7.4 K, which is about five times higher than the superconducting T_{SC} , the peaks are still easily discernable above the background. By plotting the heights of the peaks as a function of temperature, normalized by the FT background signal (Fig. 2d), we estimate the CDW onset temperature T_{CDW} to be about 10 K. This is further confirmed by the data on the second sample, where we can see that CDW peaks are largely suppressed at 10 K, with only q^2_{CDW} still visible (Fig. 2e-m), which we will discuss in more detail in subsequent paragraphs.

Spatial information can provide another important clue on the nature of the CDW suppression. We start by noting that FT of the dI/dV maps acquired at about 5 K show diffuse CDW peaks that span several reciprocal-space pixels even after Lawler-Fujita drift-correction algorithm (insets in Fig. 2a-c, Fig. 2e, inset in Fig. 3b), which generally points towards a spatially inhomogeneous order parameter. To visualize this, we Fourier-filter an integrated dI/dV map, using a process that removes all wave vectors except a narrow window around each CDW peak that is exactly 9 pixels in diameter (Fig. 3b). Nanoscale regions with periodic electronic ripples, which correspond to the CDW modulations, and regions where those modulations appear absent can be clearly observed (Fig. 3b), further supporting the notion of an inhomogeneous electronic order approaching the transition.

To gain further insight, we examine Fourier-filtered dI/dV maps of each individual CDW peak separately: q^1_{CDW} (Fig. 3d), q^2_{CDW} (Fig. 3e) and q^3_{CDW} (Fig. 3f). In the filtering process, we again select a small FT window that encompasses each individual CDW peak. We note that the overall distribution of regions where CDW is strong vs weak in our data appears comparable regardless of small variations of the filtering window size (more details on the validity of the window size can be found in Supplementary Figure 1). To quantify its local strength, we plot the intensity of each CDW peak $|q^i_{CDW}|$ (where $i = 1, 2$ or 3) as a function of position to create CDW amplitude maps (Fig. 3g-i). Our first observation is that all amplitude maps show a high level of spatial inhomogeneity, with local regions showing strong modulations dispersed within the larger matrix in which the modulations are substantially weaker. The amplitude maps of the two wave vectors related by the mirror symmetry along the y -axis, q^1_{CDW} and q^3_{CDW} , exhibit a remarkable similarity with an extremely high cross-correlation coefficient $\alpha \approx 0.7$ (Fig. 3c). Similar cross-correlation coefficients are observed between maps obtained using different sizes of the Fourier filter window (Supplementary Figure 1). Cross-correlation between the amplitude map of the remaining wave vector, $|q^2_{CDW}|$, and $|q^1_{CDW}|$ (or $|q^3_{CDW}|$) is also significant, although somewhat lower (Fig. 3c), suggesting a slightly different morphology of domains. This can be visualized by examining the maps in real space, where we can for example find regions of high $|q^2_{CDW}|$, but low $|q^1_{CDW}|$ and $|q^3_{CDW}|$ (black squares in Fig. 3d-i). This observation suggests a surprising local decoupling of individual density waves, where q^2_{CDW} becomes decoupled from mirror-symmetric q^1_{CDW} and q^3_{CDW} . This decoupling is further supported by examining the FTs of dI/dV maps at 10 K – q^2_{CDW} wave vector is still present while the other two, which were prominent at 4.8 K, are now completely suppressed (Fig. 2e-m).

To evaluate the spatial evolution of the CDW order towards T_{CDW} , we turn to the temperature dependence of the CDW amplitude maps (Fig. 4). For ease of comparison, we apply the Lawler-Fujita drift correction algorithm²¹ to all dI/dV maps, which enables us to align data acquired at different temperatures with atomic precision. This process also allows us to systematically apply an identical q -space Fourier filter across all maps examined. For simplicity, we first focus on the q^1_{CDW} peak. Visual comparison of the data sequence from 4.9 K to 6.5 K (Fig. 4a-c) reveals that nanoscale regions where CDW is the most prominent

at 4.9 K remain generally the same at the higher temperature. However, amplitude within these nanoscale regions has decreased leading to the appearance that they have shrunk (Fig. 4d-f), consistent with the global suppression of CDW in Fig. 2. Cooling the system back down to the starting temperature of 4.9 K yields the CDW amplitude maps that are virtually indistinguishable from those before the thermal cycle (Fig. 4h). Multiple consecutive thermal cycles paint the same picture of static CDW patches that get suppressed with temperature and expand again upon cooling down (Fig. 4h). The striking similarity of the locations of CDW patches at different temperature is confirmed by the high cross-correlation coefficient (Fig. 4g).

Complementary to temperature dependence, we study how the CDW is suppressed by magnetic field. Previous experiments revealed an intriguing suppression of the CDW in the superconducting state coinciding with the suppression of superconductivity, suggesting an intimate connection between the two¹⁸. Here we apply magnetic field at 4.8 K, well above the superconducting transition of UTe_2 . The field is applied at 3 degrees with respect to the direction perpendicular to the sample surface (Figure 5a,b). We find that the height of CDW peaks slowly decreases with applied magnetic field (Fig. 5c-f). For example, q^1_{CDW} lowers by about 35% from 0 T to 11 T, but remains well above the background (Fig. 5c,e). This suggests a critical field substantially higher than 11 T. The trend is remarkably consistent with the CDW evolution in the superconducting state¹⁸, although we are in the temperature regime that is three times higher than superconducting T_{SC} . To gain spatial information, we extract CDW amplitude maps as a function of magnetic field similarly to our analysis in Figures 3 and 4. This analysis leads us to two main conclusions. First, CDW patches are again suppressed by the shrinkage of local regions (Fig. 5g,h). Second, CDW puddles revert back to the original morphology after the field is removed (Fig. 5g,h).

Discussion:

Our work reveals how intertwined density waves in a rare spin-triplet superconductor UTe_2 get suppressed with temperature, by first forming short-range nanoscale regions with charge modulations embedded within areas where modulations can no longer be observed. Interestingly, we find that the three CDW wave vectors locally decouple. Based on the energy-dependence and the temperature-suppression, we conclude that q^2_{CDW} along the mirror symmetry axis is distinct compared to the other two wave vectors. This in turn suggests a superposition of at least two independent density waves: unidirectional, or “smectic”, density wave associated with q^2_{CDW} and a bi-directional combination of mirror-symmetric q^1_{CDW} and q^3_{CDW} . It is possible that q^1_{CDW} and q^3_{CDW} would also behave as individual smectic density waves given the different field dependence reported in Ref.¹⁸, although as we discover in Figure 3, they appear to be spatially intertwined. We note that vortex-like discontinuities seen between regions with strong modulations in Fourier filtered data, also recently reported in Ref.²² (examples of two such features rotated by π with respect to each other are denoted by arrows in Fig. 3d) can dramatically change depending on the size of the filtering window as CDW peaks become less prominent. Moreover, these features routinely appear in the Fourier-filtered data of spatially inhomogeneous orders in other systems (Supplementary Figure 2). Lastly, as these discontinuities always appear in regions with near-zero amplitude of the order parameter, which is generally below the FT noise threshold, we disregard them in our analysis.

Our experiments also reveal a remarkable repeatability of the morphology of nanoscale CDW regions by magnetic field or temperature cycling. In many materials, atomic-scale crystal imperfections are often responsible for electronic inhomogeneity^{23–25}. Future experiments should explore to what extent

accidental impurities or defects could account for the fragmentation or pinning of the charge modulations. This would be especially important to determine given the variation in the properties of nominally stoichiometric crystals of UTe_2 , where chemical inhomogeneity could be the natural culprit but defects responsible for this are yet to be identified.

Magnetic field suppression of the density waves provides narrow constraints on their origin. The possibility of intrinsic PDW, which melts into a CDW above T_{sc} , was largely supported by the critical magnetic field of the CDW comparable to that of the superconducting critical fields¹⁸. In our experiments, we find that similarly high magnetic fields are necessary to suppress CDW well above T_{sc} (Fig. 5), thus making the immediate connection to superconductivity less obvious. On the other hand, our SI-STM data, which reveal a new 10-12 K temperature scale associated with density waves, provide a fresh clue. Both thermal expansion coefficient data²⁶ and resistivity measurements²⁷ reveal features in their data near the same temperature. In particular, a recent pressure study demonstrates that this resistivity feature coincides with the eventual stabilization of the long-range magnetic order; as such, it is attributed to a magnetic energy scale indicative of magnetic fluctuations²⁷. This could provide the first plausible link between surface detection of density waves and bulk experiments. This connection, combined with magnetic-field sensitivity of the charge modulations in both superconducting¹⁸ and non-superconducting states (Fig. 5), could point towards the origin of charge modulations in underlying spin fluctuations, which should be tested more directly in future spin-sensitive experiments.

Methods

Bulk single crystals of UTe_2 are grown using the method described in Ref. ¹⁰. UTe_2 crystals are transported from NIST to BC in a sealed glass vile filled with inert gas to prevent air degradation. The vile is opened in an argon glove box at BC, where the sample is glued to an STM sample holder, and a cleave bar is then attached to the sample using silver epoxy. We transfer the prepared sample from the glove box to an ultra-high vacuum load lock within seconds, and cold-cleave it before putting it into the microscope. STM data was acquired using a customized Unisoku USM1300. Spectroscopic measurements were performed using a standard lock-in technique with 910 Hz frequency. The STM tips used were home-made chemically etched tungsten tips. For the ease of comparison of data acquired at different temperatures and to standardize the Fourier filter windows applied in the analysis, we apply the Lawler–Fujita drift-correction algorithm²¹ to our data. This process shifts and aligns the atomic Bragg peaks to be confined to the same individual pixels. Identification of commercial equipment does not imply endorsement by NIST.

References

1. Fradkin, E., Kivelson, S. A. & Tranquada, J. M. Colloquium : Theory of intertwined orders in high temperature superconductors. *Rev. Mod. Phys.* **87**, 457–482 (2015).
2. Ruan, W. *et al.* Visualization of the periodic modulation of Cooper pairing in a cuprate superconductor. *Nat. Phys.* **14**, 1178–1182 (2018).
3. Hamidian, M. H. *et al.* Detection of a Cooper-pair density wave in $\text{Bi}_2\text{Sr}_2\text{CaCu}_2\text{O}_{8+x}$. *Nature* **532**, 343–347 (2016).
4. Edkins, S. D. *et al.* Magnetic field–induced pair density wave state in the cuprate vortex halo. *Science* **364**, 976–980 (2019).
5. Zhao, H. *et al.* Smectic pair-density-wave order in $\text{EuRbFe}_4\text{As}_4$. *Nature* **618**, 940–945 (2023).

6. Liu, Y. *et al.* Pair density wave state in a monolayer high- T_c iron-based superconductor. *Nature* **618**, 934–939 (2023).
7. Chen, H. *et al.* Roton pair density wave in a strong-coupling kagome superconductor. *Nature* **599**, 222–228 (2021).
8. Zhao, H. *et al.* Cascade of correlated electron states in the kagome superconductor CsV_3Sb_5 . *Nature* **599**, 216–221 (2021).
9. Li, H. *et al.* Small Fermi pockets intertwined with charge stripes and pair density wave order in a kagome superconductor. *ArXiv* 2303.07254 (2023).
10. Ran, S. *et al.* Nearly ferromagnetic spin-triplet superconductivity. *Science* **365**, 684–687 (2019).
11. Aoki, D. *et al.* Unconventional superconductivity in UTe_2 . *J. Phys. Condens. Matter* **34**, 243002 (2022).
12. Hayes, I. M. *et al.* Multicomponent superconducting order parameter in UTe_2 . *Science* **373**, 797–801 (2021).
13. Sundar, S. *et al.* Coexistence of ferromagnetic fluctuations and superconductivity in the actinide superconductor UTe_2 . *Phys. Rev. B* **100**, 140502 (2019).
14. Duan, C. *et al.* Resonance from antiferromagnetic spin fluctuations for superconductivity in UTe_2 . *Nature* **600**, 636–640 (2021).
15. Thomas, S. M. *et al.* Evidence for a pressure-induced antiferromagnetic quantum critical point in intermediate-valence UTe_2 . *Sci. Adv.* **6**, 1–8 (2020).
16. Nakamine, G. *et al.* Superconducting Properties of Heavy Fermion UTe_2 Revealed by ^{125}Te -nuclear Magnetic Resonance. *J. Phys. Soc. Japan* **88**, 113703 (2019).
17. Ran, S. *et al.* Extreme magnetic field-boosted superconductivity. *Nat. Phys.* **15**, 1250–1254 (2019).
18. Aishwarya, A. *et al.* Magnetic-field-sensitive charge density waves in the superconductor UTe_2 . *Nature* **618**, 928–933 (2023).
19. Gu, Q. *et al.* Detection of a pair density wave state in UTe_2 . *Nature* **618**, 921–927 (2023).
20. Jiao, L. *et al.* Chiral superconductivity in heavy-fermion metal UTe_2 . *Nature* **579**, 523–527 (2020).
21. Lawler, M. J. *et al.* Intra-unit-cell electronic nematicity of the high- T_c copper-oxide pseudogap states. *Nature* **466**, 347–351 (2010).
22. Aishwarya, A. *et al.* Visualizing the melting of the charge density wave in UTe_2 by generation of pairs of topological defects with opposite winding. *Arxiv* 2306.09423 (2023).
23. Zeljkovic, I. *et al.* Imaging the impact of single oxygen atoms on superconducting $\text{Bi}_{2+y}\text{Sr}_{2-y}\text{CaCu}_2\text{O}_{8+x}$. *Science* **337**, 320–3 (2012).
24. Zeljkovic, I. & Hoffman, J. E. Interplay of chemical disorder and electronic inhomogeneity in unconventional superconductors. *Phys. Chem. Chem. Phys.* **15**, 13462–78 (2013).
25. Zhao, H. *et al.* Imaging antiferromagnetic domain fluctuations and the effect of atomic scale

- disorder in a doped spin-orbit Mott insulator. *Sci. Adv.* **7**, abi6468 (2021).
26. Thomas, S. M. *et al.* Spatially inhomogeneous superconductivity in UTe_2 . *Phys. Rev. B* **104**, 224501 (2021).
 27. Kim, H. *et al.* Tuning a magnetic energy scale with pressure in UTe_2 . *Arxiv* 2307.00180 (2023).

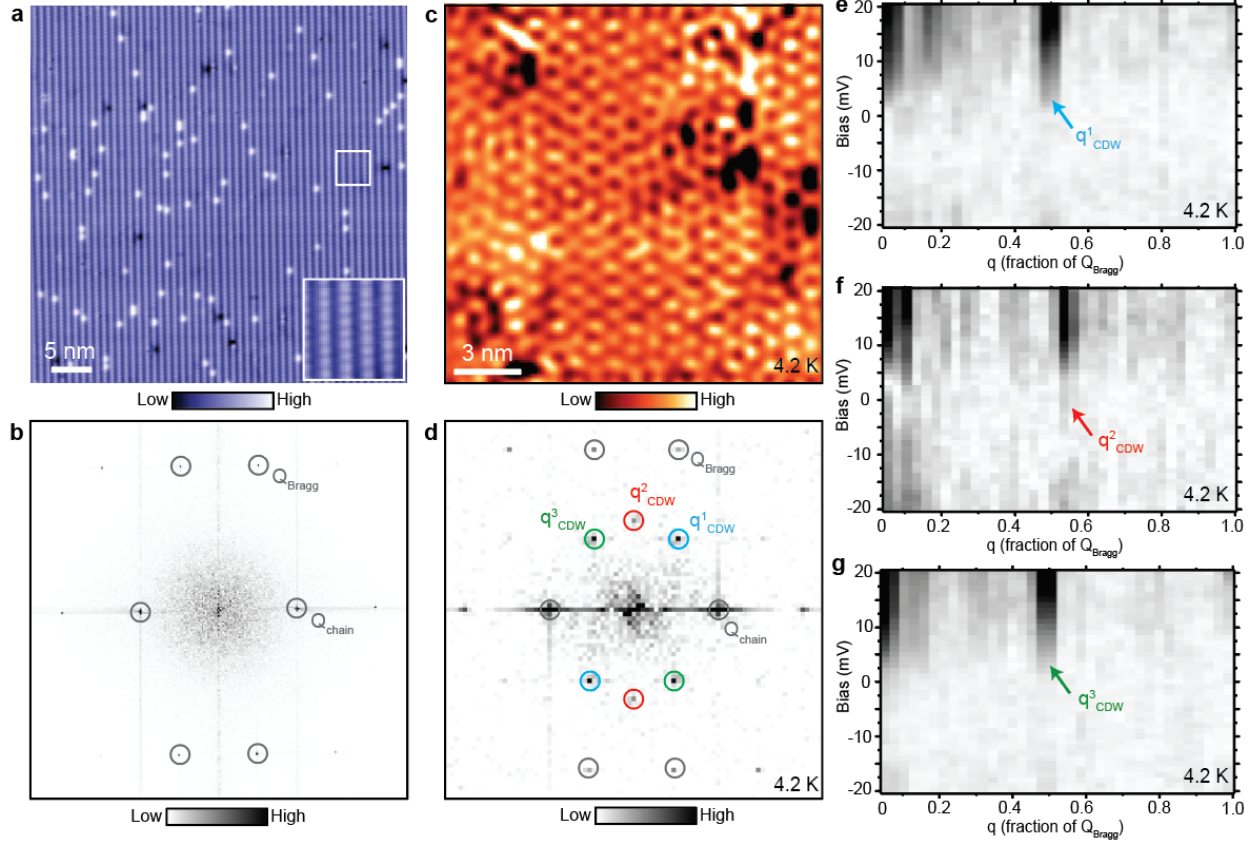


Figure 1. Characterization of the UTe_2 surface and the non-dispersive charge modulation peaks. (a) Atomically-resolved scanning tunneling microscopy (STM) topograph of UTe_2 (0-11) surface with bright rows of Te atoms positioned along the crystal a -axis. Inset in (a) shows the zoomed-in topograph over the small white square. (b) Fourier transform (FT) of the STM topograph in (a). Te Bragg peaks (Q_{Bragg}) and the unidirectional chain peaks (Q_{chain}) are circled. (c) Fourier filtered single-layer dI/dV map on the same UTe_2 (0-11) surface showing the characteristic charge density wave (CDW) pattern, and (d) its associated FT. Three different CDW peaks q^1_{CDW} , q^2_{CDW} , and q^3_{CDW} are circled in the FT in (d) in blue, red and green, respectively. (e-g) FT linecuts, starting from the center of the FT through each of the three CDW peaks, as a function of energy. It can be seen that the position of the three CDW peaks is not dependent on energy. STM setup condition: $V_{\text{sample}} = -20$ mV, $I_{\text{set}} = 100$ pA (a); $V_{\text{sample}} = 20$ mV, $I_{\text{set}} = 40$ pA (c); $V_{\text{sample}} = -20$ mV, $I_{\text{set}} = 40$ pA, $V_{\text{exc}} = 3$ mV (e-g).

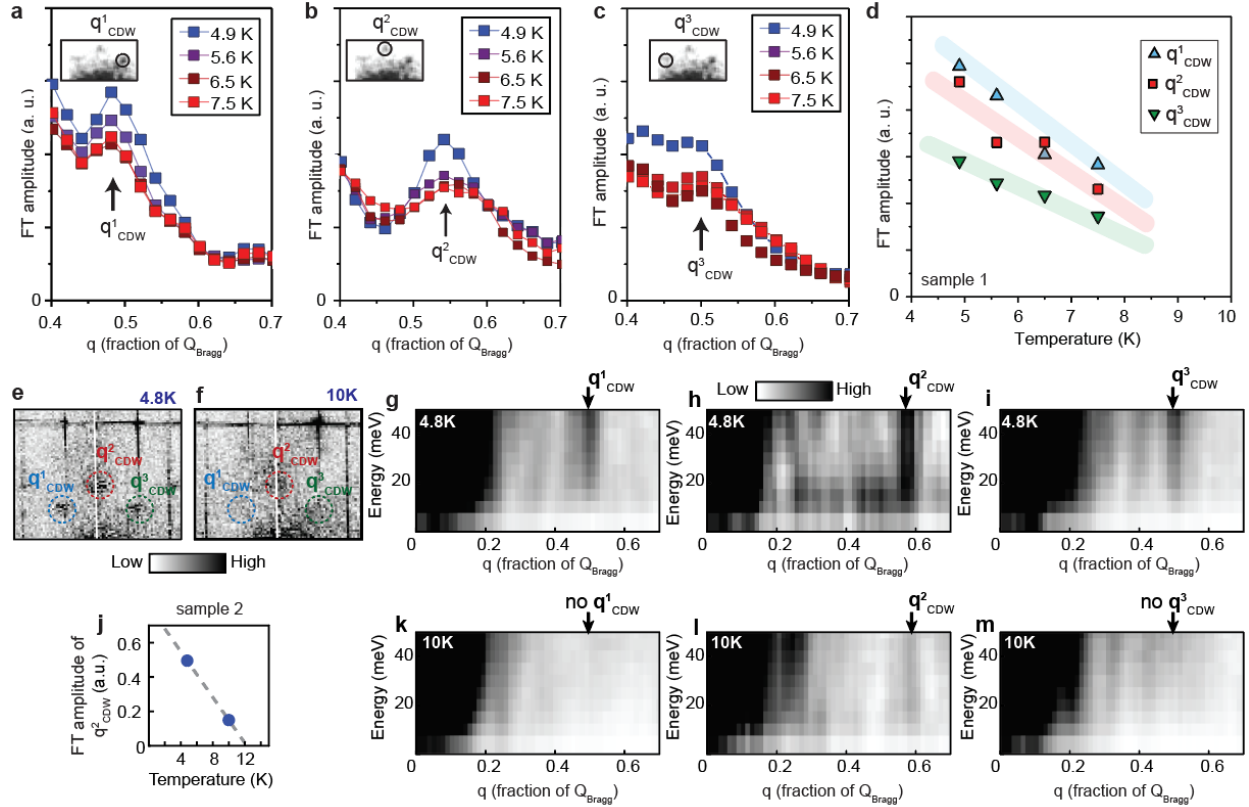


Figure 2. Temperature-dependence of the charge density wave modulations. (a-c) Fourier transform (FT) linecuts of the dI/dV map acquired at 40 mV, starting from the center of the FT, through the three CDW peaks: (a) q^1_{CDW} , (b) q^2_{CDW} , and (c) q^3_{CDW} on sample 1. Suppression of the CDW peaks is apparent with increasing temperature. Insets in (a-c) show the relevant portion of the FT, with the corresponding wave vector that is plotted circled. (d) Plot of the background-subtracted height (FT amplitude) of the Gaussian fits to each peak in the temperature-dependent linecuts in (a-c). Blue, red and green lines represent visual guides for each of the three CDW peak amplitude dispersions, which seem to approach zero amplitude at about 10 K. (e,f) FT of dI/dV map acquired at 50 mV on sample 2 at (e) 4.8 K and (f) 10 K. The positions of three CDW peaks are circled. (g-i) FT linecuts, starting from the center of the FT through each of the three CDW peaks, as a function of energy at 4.8 K. (k-m) FT linecuts, starting from the center of the FT through each of the three CDW peaks, as a function of energy at 10 K. q^1_{CDW} and q^3_{CDW} cannot be resolved at 10 K, while q^2_{CDW} still shows up with weakened magnitude. (j) FT peak height of q^2_{CDW} as a function of temperature extracted from (e,f).

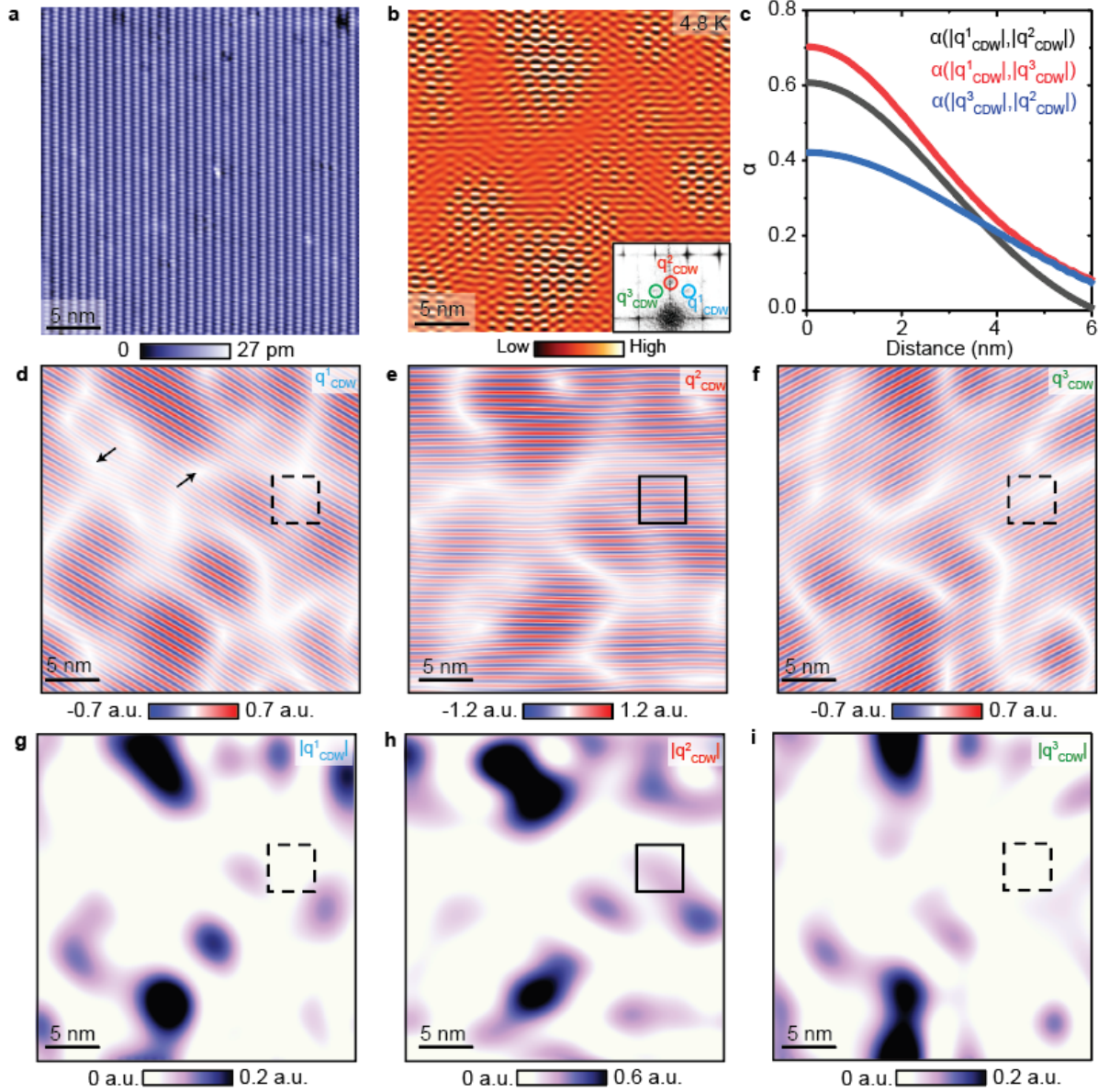


Figure 3. Spatial inhomogeneity and local decoupling of the CDW modulations. (a) STM topograph and (b) filtered integrated dI/dV map (adding 4 layers acquired at 35 mV, 40 mV, 45 mV and 50 mV) over the (0-11) surface of UTe_2 . Fourier filtering is done by removing all wave vectors except 9 pixel diameter centered at each q^1_{CDW} , q^2_{CDW} and q^3_{CDW} . Inset in (b) is the relevant portion of the Fourier transform of the integrated dI/dV map, with CDW peaks circled in blue, red and green. (c) Cross-correlation coefficients between the three CDW amplitude maps shown in (g-i). (d-f) Fourier filtered maps extracted from (a) by selectively keeping only a narrow circular FT window centered at (d) q^1_{CDW} , (e) q^2_{CDW} and (f) q^3_{CDW} . Two arrows in (d) point to apparent dislocations that routinely appear in the areas of low CDW amplitude. (g-i) CDW amplitude maps extracted from corresponding images in (d-f), showing the local height of each CDW wave vector. Black squares in (d-i) mark the same position on the sample with strong (solid line) and weak (dashed line) modulations. STM setup conditions: $V_{sample} = 50$ mV, $I_{set} = 300$ pA, $V_{exc} = 10$ mV.

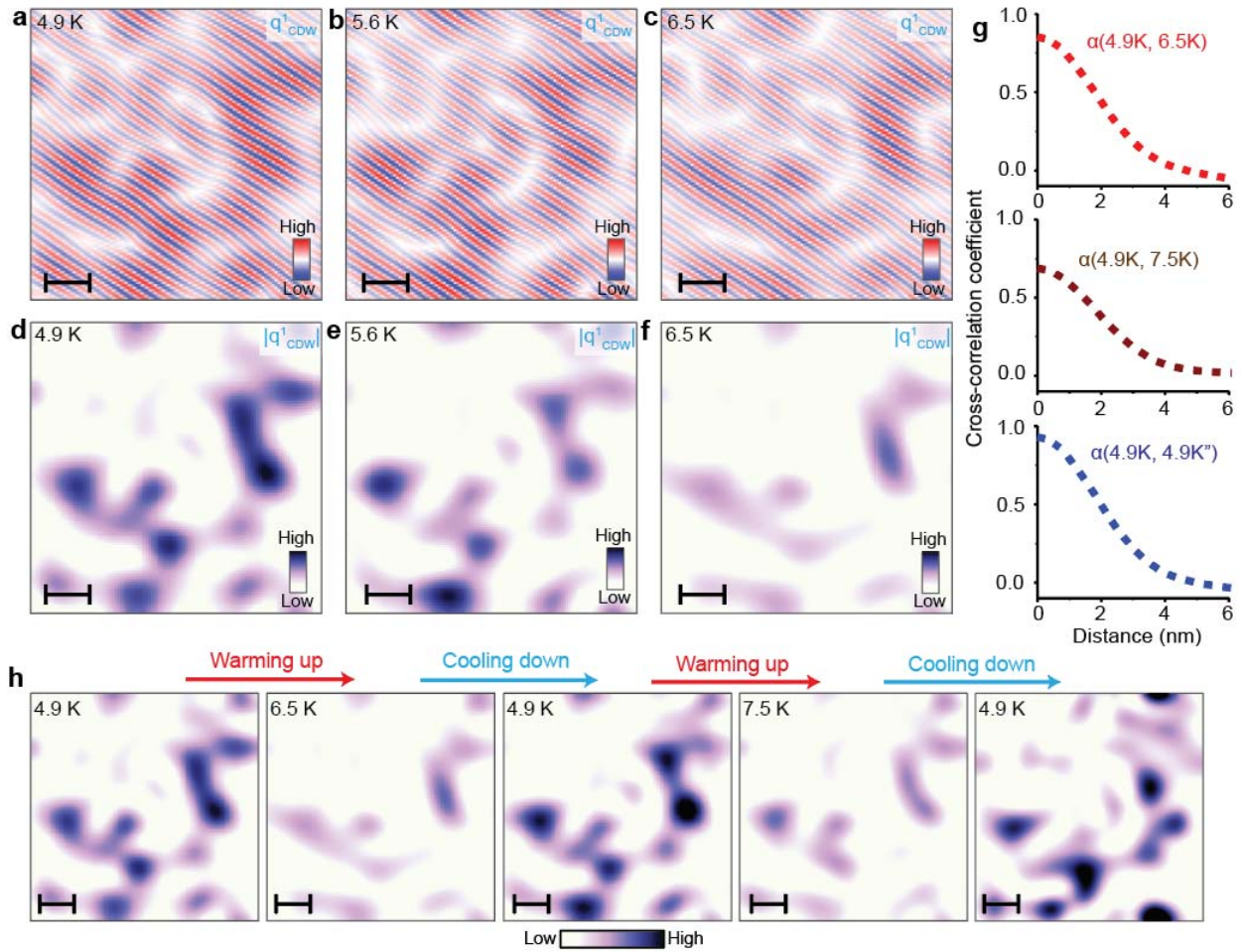


Figure 4. Temperature dependence of the CDW spatial inhomogeneity and robustness to thermal cycles. (a-c) Fourier filtered dI/dV maps showing the temperature dependence of the inhomogeneity of q^1_{CDW} , and (d-f) associated amplitude maps. (g) Radially-averaged cross-correlation coefficient α between pairs of different amplitude maps: $\alpha(4.9K, 6.5K)$ (red, top curve), $\alpha(4.9K, 7.5K)$ (brown, middle curve), and $\alpha(4.9K, 4.9K'')$ (blue, bottom curve). (h) Thermal cycling sequence of amplitude maps associated with q^1_{CDW} taken at the same STM setup conditions. The scale bar in all images is 3 nm. STM setup condition: $V_{sample} = 40$ mV, $V_{exc} = 100$ mV, $I_{set} = 160$ pA.

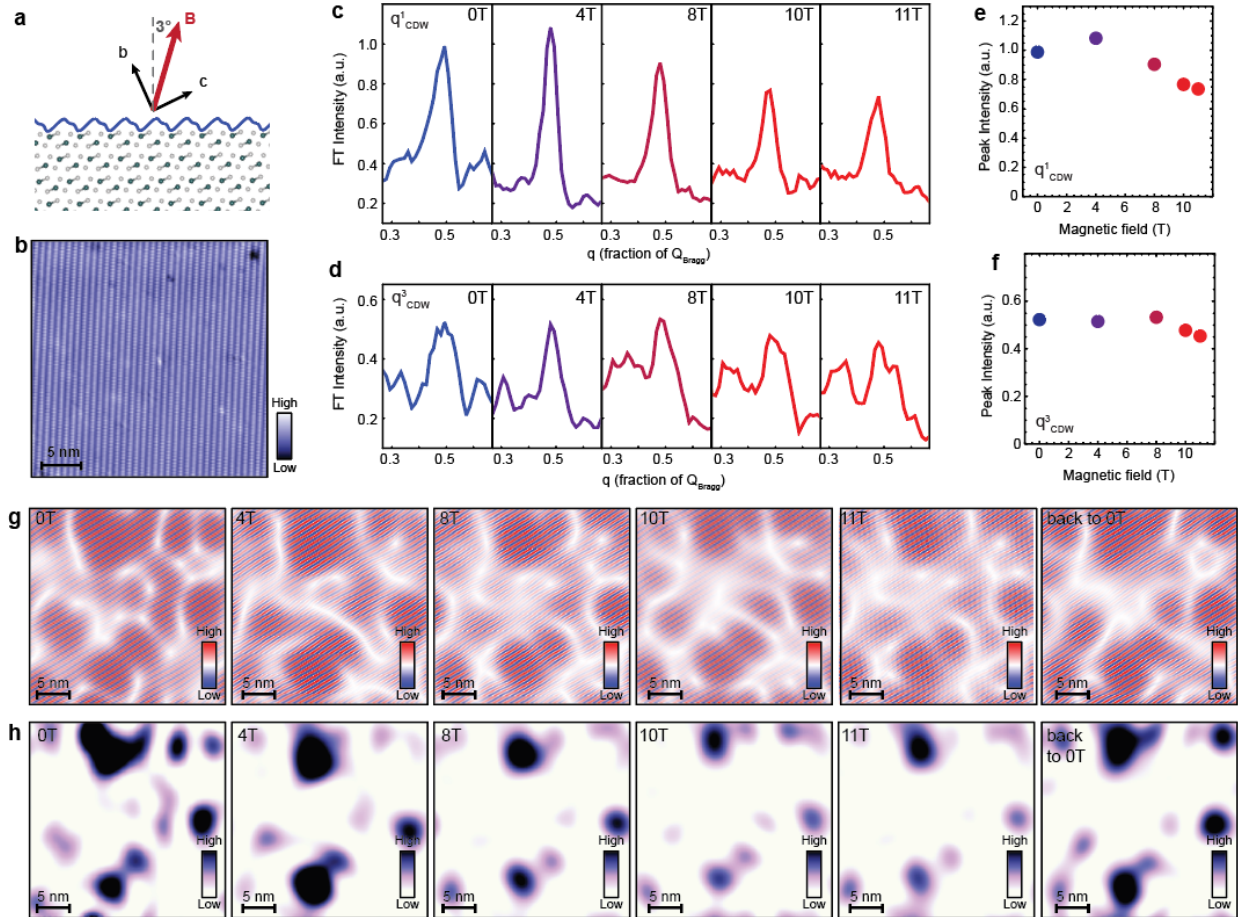


Figure 5. CDW suppression by magnetic field in the normal state of UTe_2 and field sensitivity of spatial inhomogeneity. (a) Schematic of the magnetic field direction applied 3 degrees with respect to the direction perpendicular to the sample surface imaged by STM. This small misalignment is due to accidental sample tilt during the gluing process, and it is determined from the background slope in raw STM topographs. (b) STM topograph of the region of the sample where the data was taken. (c,d) Fourier transform (FT) linecuts from the center of the dI/dV map FT through (c) q^1_{CDW} and (d) q^3_{CDW} peaks as a function of magnetic field. Sensitivity of the peak heights to large magnetic fields is observed. (e,f) Peak heights extracted from (c,d) plotted as a function of magnetic field. (g) Fourier filtered dI/dV maps including only the q^1_{CDW} peak (encompassing a 9 pixel diameter around the peak center), and (h) associated amplitude maps. STM setup condition: $V_{sample} = -50\text{ mV}$, $I_{set} = 300\text{ pA}$, $V_{exc} = 10\text{ mV}$. Data was taken at 4.8 K.